

Measurement and assignment of the size-dependent optical spectrum in CdSe quantum dots

D. J. Norris* and M. G. Bawendi

Massachusetts Institute of Technology, 77 Massachusetts Avenue, Cambridge, Massachusetts 02139

(Received 2 March 1995)

We use photoluminescence excitation to study the electronic spectrum of CdSe quantum dots ranging from ~ 12 to ~ 53 Å in radius. We follow the size evolution of ten quantum dot absorption features. Comparison of the spectra with theoretical predictions allows us to confidently assign six of these transitions. We discuss the most likely assignments for the remaining four. We find that the $n_h S_{3/2} 1S_e$ and $n_h S_{1/2} 1S_e$ transitions dominate the spectra, accounting for half of the observed features. Our size-dependent data exhibit two strong avoided crossings, demonstrating the importance of valence-band structure in the description of the excited states. [S0163-1829(96)07120-2]

I. INTRODUCTION

A primary motivation in the study of nanometer-scale semiconductor crystallites (or quantum dots) is to understand how the size of a semiconductor material influences its electronic properties. Quantum dots provide an opportunity to study the evolution of electronic behavior in a size regime intermediate between the molecular and bulk limits of matter. Interesting and strongly size-dependent optical properties arise in these materials when the quantum dot is small compared to the natural length scale of the electron-hole pair, the exciton Bohr radius.^{1,2} In this limit, referred to as the strong confinement regime,¹ the electron and hole wave functions experience three-dimensional quantum confinement due to the dot boundary. The confinement induces quantization of the bulk electronic bands such that quantum dots, sometimes called “artificial atoms,” have discrete electronic transitions that shift to higher energies with decreasing size. These basic properties have been demonstrated by numerous optical studies on II-VI semiconductor quantum dots, such as CdS and CdSe.^{3–23}

However, one of the original and basic experimental questions about quantum dots—how their electronic spectra evolve with size in the strong confinement regime—remains largely unanswered. Early work on this question^{3–10} was constrained by difficulties in preparing high-quality, monodisperse samples. Inhomogeneities such as distributions in size and shape that conceal the higher transitions prevented a more complete investigation. Early efforts were limited both in the number of sizes as well as in the number of states that were investigated. More recent studies,^{11–14} which do examine quantum dots of sufficient quality to resolve many of the higher states, are restricted to one^{11–13} or a few¹⁴ sizes.

Methods in quantum dot fabrication now allow the size dependence question to be addressed more satisfactorily. We prepare colloidal CdSe quantum dots with a synthetic procedure¹⁵ which provides extremely monodisperse ($<5\%$ rms) II-VI quantum dots ranging from ~ 7.5 to ~ 60 Å in radius, a size range that spans the strong confinement regime for CdSe.²⁴ In a previous Letter¹⁶ we used transient differential absorption (TDA) spectroscopy to report preliminary results on the size-dependent spectrum of CdSe quantum dots in the strong confinement regime. Although TDA effectively

increases the resolution of the spectrum by optically selecting and bleaching a subset of the quantum dots, competition between bleach features and induced absorptions complicates the analysis. Here we present a more detailed investigation of the size-dependent spectrum using photoluminescence excitation (PLE) spectroscopy that avoids this situation. We examine a much larger sample series and study the evolution of ten quantum dot absorption features as a function of dot radius.

II. EXPERIMENT

We prepare CdSe quantum dots according to the method of Ref. 15. In this procedure the wet chemical synthesis is followed by size-selective precipitation to further narrow the size distribution. Samples with very narrow size distributions ($<5\%$ rms) are obtained that contain slightly prolate (aspect ratio 1.0–1.3), near defect-free, wurtzite crystallites with well-passivated surfaces.^{15,25,26} The dots exhibit strong band-edge luminescence with a quantum yield (at 10 K) greater than 0.1 and measured as high as 0.9. The intensity of deep trap emission, which dominates the luminescence behavior of dots prepared by many other methods, is size dependent in our samples. Negligible in our largest dots, it slowly increases with decreasing size and becomes significant in our smallest size samples.

We study 24 samples with mean radii ranging from ~ 12 to ~ 53 Å.²⁷ Three of the samples were used in our previous TDA results.^{16,22} These older samples were isolated from the growth solution and redispersed in tri-*n*-butyl-phosphine (TBP) with *o*-terphenyl added (200 mg/ml) to form an optically clear organic glass at cryogenic temperatures. Most samples, however, are isolated and redispersed in *n*-hexane with a small amount of tri-*n*-octyl-phosphine (TOP). An excess of TBP or TOP, both surface capping groups, maintains surface passivation and preserves the high photoluminescence quantum yield.²⁸ While our preparation method produces almost any desired dot diameter, certain sizes (“magic sizes”) are preferred in the growth process.¹⁵ Small dots (with their first absorption peak between ~ 2.58 and ~ 2.48 eV) that are between two magic sizes seem to be the least stable. Over weeks their spectra broaden when stored at room temperature, presumably due to continued slow

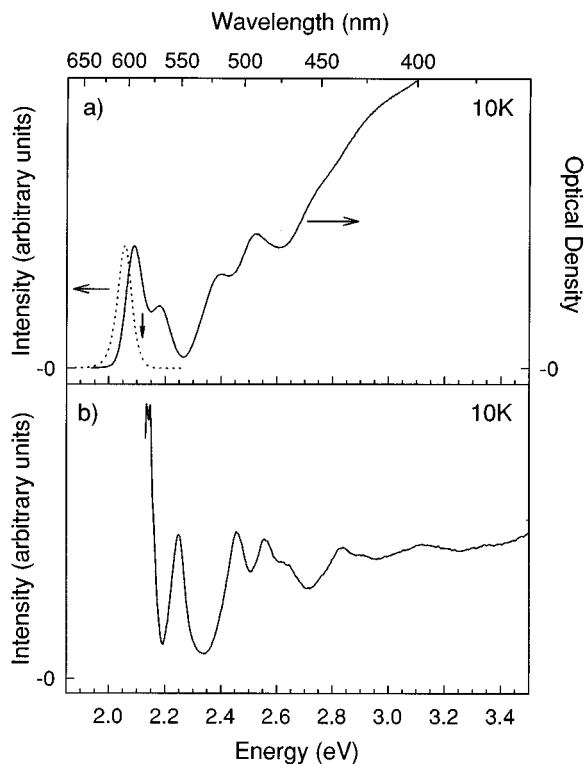


FIG. 1. (a) Absorption (solid line) and photoluminescence (dashed line) spectra for ~ 28 -Å-radius quantum dots. In luminescence the sample was excited at 2.655 eV (467.0 nm). The downward arrow marks the emission position used in PLE. (b) PLE scan for ~ 28 -Å-radius dots.

growth. To avoid this complication we record PLE spectra for the six smallest dot sizes immediately after preparation with the dots still in the reaction solution. Larger samples (with the first absorption peak < 2.48 eV) are stable for much longer (months to years) periods of time.

For optical measurements each sample is placed between sapphire flats separated by a 0.5-mm-thick Teflon spacer and mounted in a helium cryostat. All spectra are obtained at 10 K. We record photoluminescence and PLE spectra using a SPEX Fluorolog-2 spectrofluorometer. This instrument consists of two double (0.22 m) spectrometers. The first selects the desired excitation energy from the emission of a xenon arc lamp. The second chooses the emission energy detected by a photomultiplier tube (R928). Under experimental conditions for PLE the combined resolution of our instrument was ~ 3 meV [full width at half maximum (FWHM)].

III. RESULTS

Although the quality of our samples is among the highest reported, inhomogeneities remain that broaden absorption features and conceal transitions. PLE reduces these effects by optically selecting a subset of the sample distribution.¹¹ In Fig. 1 we demonstrate this technique along with absorption and luminescence spectra for ~ 28 Å radius dots.²⁷ When excited well above the first transition, emission occurs from the entire sample distribution and a broad luminescence band is observed [FWHM 56 meV, dashed line in Fig. 1(a)]. However, fluorescence line narrowing experiments^{11,17,18} show

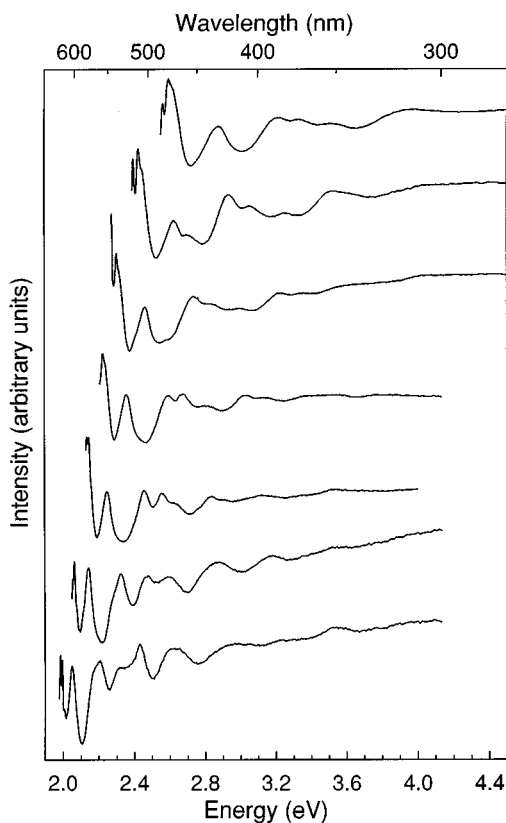


FIG. 2. Normalized PLE scans for seven different size quantum dot samples. Size increases from top to bottom and ranges from ~ 15 to ~ 43 Å in radius. In many scans a broad lamp artifact appears at ~ 3.5 eV. This feature was ignored in the data analysis.

that “single dot” emission is characterized by a vibrational (LO phonon) progression with much narrower features (FWHM ~ 8 meV). The difference between the single dot and inhomogeneous emission linewidths allows PLE to select a specific portion of the sample distribution. By monitoring a narrow spectral band of the full luminescence while scanning the excitation energy, PLE reveals absorption features with inhomogeneous broadening greatly reduced. As seen in Fig. 1, transitions that overlap in direct absorption [Fig. 1(a)] are resolved by PLE [Fig. 1(b)]. Due to this increase in resolution, PLE has become a standard technique to obtain quantum dot absorption information.^{11,19–21}

To obtain PLE data for each sample we first measure its broad luminescence band. Since features are most efficiently resolved in PLE when the emission is monitored on the blue edge of the luminescence,¹¹ we then generally select an emission energy where the blue edge intensity is $\sim \frac{1}{3}$ of the peak height. For example, in Fig. 1(b) we use the energy denoted by the downward pointing arrow in Fig. 1(a). We then record PLE spectra at emission positions slightly to the red and to the blue of this original energy (generally ± 5 nm). This allows us to increase the number of “sizes” that are investigated since the emission energy chosen in PLE decides which subset of the sample distribution is probed. Below we analyze 53 different “sizes” generated from 24 samples.

In Fig. 2 we show PLE spectra for seven of our samples, ranging from ~ 15 to ~ 43 Å in mean radius.²⁷ The spectra

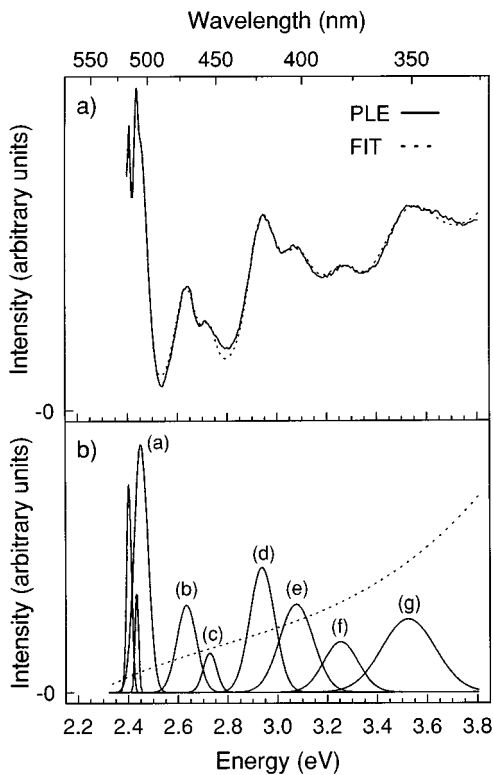


FIG. 3. (a) Demonstration of the fitting procedure used to extract PLE peak positions. The PLE scan (solid line) is compared to the fit (dashed line) for a $\sim 18\text{-}\text{\AA}$ -radius sample. The structure on the first absorption is clearly visible in this plot. (b) The individual Gaussian components (solid lines) and the cubic background (dashed line), which combine to form the fit. The first absorption peak is decomposed into two narrow features slightly to the red of a broader absorption peak. For comparison the peaks are labeled as in Fig. 4.

are arranged in order of increasing dot size (top to bottom) and quantum confinement clearly shifts the transitions blue with decreasing size. The high quality of our dots allows us to resolve as many as eight absorption features in a single spectrum. We also observe additional structure on the first absorption peak, as seen in Fig. 2. In most spectra a narrow line with LO phonon replicas is observed on top of a much broader feature. Similar narrow and broad substructure is seen in TDA experiments.^{11,16,22} These additional features, which are consistent with band-edge exciton fine structure, are discussed in a companion paper.²⁹ Here we focus solely on the higher excited states.

Figure 2 presents a portion of our complete experimental data set. PLE spectra for each of our 24 samples are presented in Ref. 30. To quantify this information and describe the quantum dot spectrum as a function of size we extract the energies of the quantum dot transitions using the fitting procedure demonstrated in Fig. 3. Each PLE spectrum is fit with a sum of Gaussians using standard nonlinear least-squares methods.³¹ To model the continuumlike nature of underlying transitions that are not resolved we use a cubic background curve [dashed line in Fig. 3(b)]. The narrow and broad components of the lowest transition, mentioned above, are clearly observed in Fig. 3. The broad component, which car-

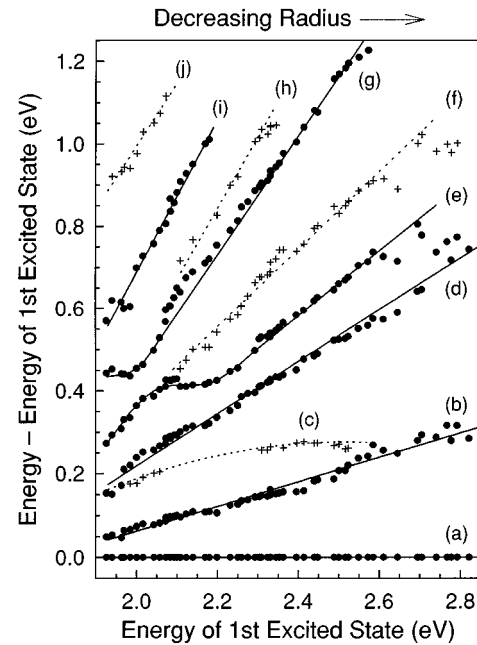


FIG. 4. Transition energies (relative to the first excited state) vs the energy of the first excited state. Peak positions are extracted from PLE data as described in the text and shown in Fig. 3. This plot shows all of our PLE data, including several PLE scans for each of our 24 samples. Strong (weak) transitions are denoted by circles (crosses). The solid (dashed) lines are visual guides for the strong (weak) transitions to clarify their size evolution.

ries most of the oscillator strength, is used for the energy of the first transition in our analysis.

In agreement with previous work, our fits show that transition linewidths increase with increasing energy^{11,19} (Fig. 3) and decreasing size.^{16,19} Rough estimates of oscillator strength based on our fits also confirm that excited-state transitions are comparable to or weaker than the first transition, as expected from theory.^{14,32} Unfortunately, a more quantitative analysis of the transition strengths is prevented by the presence of the unresolved states, modeled by the cubic background. In addition, since PLE represents a combination of absorption and emission behavior, a detailed knowledge of the emission quantum yield for each transition would be required to quantify the absorption strength of the states observed in PLE.¹⁹

The final results of the fitting procedure for our entire data set are shown in Fig. 4. In this plot we choose what may seem to be unusual axes. The x axis is the energy of the first excited state. Energy is more easily and precisely measured than dot size and is also a better size-dependent label. Using the average radius as determined by transmission electron microscopy as the x axis would introduce significant size measurement error, both systematic and random. In addition, the mean sizes obtained would not represent the subset of the size distribution that is measured in PLE. The energy of the first transition better describes those dots that are actually probed. The y axis is energy relative to the first excited state.

Figure 4 summarizes our experimental results and shows the size-dependent spectrum of CdSe quantum dots in the strong confinement regime. All of our data (53 “sizes”) are shown, including several PLE scans per sample, as discussed

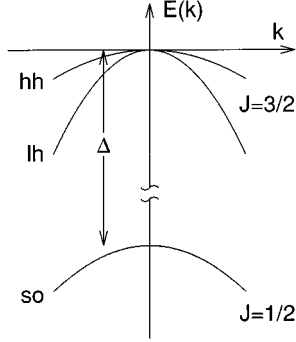


FIG. 5. Illustration of the valence band for diamond-type semiconductors near $k=0$, which is split into heavy hole (hh), light hole (lh), and split-off (so) hole subbands. Δ is the spin-orbit coupling. The valence-band structure of CdSe with cubic (zinc-blende) symmetry is well approximated by this structure.

above. Our spectra describe the size evolution of ten quantum dot absorption features, labeled (a) through (j) in Fig. 4. Strong (weak) features are denoted by circles (crosses) with solid (dashed) lines drawn as visual guides to clarify their size evolution. We note that due to complications with overlapping induced absorptions, the four weak transitions in Fig. 4 (dashed lines) were not observed in our previous TDA results.¹⁶

IV. DISCUSSION

A. Theoretical overview

The size range studied in this paper is in the strong confinement regime^{1,2} where the confinement energy of the electron and hole is much larger than their Coulomb interaction. The carriers can then be treated independently and the Coulomb term included as a perturbation. Working in the strong confinement limit allows the theoretical problem to be conveniently divided into separate electron and hole components. The electron and hole wave functions are each described by the product of a unit cell basis function and an envelope function, which satisfies the spherical boundary condition. Since the unit cell components are assumed identical to the bulk, quantum dot theory focuses on determining the envelope functions of the individual carriers.

Early theoretical work^{1,2} assumed a simple two-band isotropic effective mass model to approximate the bulk valence and conduction bands. When confined by an infinite potential barrier at the dot boundary, each carrier is described by a ‘‘particle-in-a-sphere’’ envelope function, the product of a spherical harmonic and a spherical Bessel function. The hole (electron) envelope function is labeled by its angular momentum L_h (L_e), and radial quantum number n_h (n_e). The total quantum dot wave function is the product of the individual hole and electron components. In this model the first excited state is written as $1S_h1S_e$, with the hole and electron both in the first ($n_h=1$, $n_e=1$) S -like ($L=0$) envelope function.

In general the valence band of diamond-type semiconductors, illustrated in Fig. 5, is more complicated than the simple parabolic band assumed above.³³ The valence band, which arises from p atomic orbitals, has an inherent sixfold degeneracy

(including spin) at $k=0$. When spin-orbit coupling (Δ) is strong this degeneracy is split into a fourfold degenerate $p_{3/2}$ band (Γ_8) and a ‘‘split-off’’ twofold degenerate $p_{1/2}$ band (Γ_7). (The subscripts, $3/2$ or $1/2$, describe the total unit cell angular momentum, $J=l+s$.) Away from $k=0$ the $J=3/2$ band splits further into the heavy-hole ($J_m=\pm 3/2$) and light-hole ($J_m=\pm 1/2$) bands, both doubly degenerate.³³

More recent quantum dot theoretical work^{14,32,34–37} considers the valence-band degeneracy and includes a better description of the CdSe valence band. For convenience theory assumes a cubic (zinc-blende) crystal lattice. [Below we discuss the effects of the correct hexagonal (wurtzite) lattice.] In this case the CdSe valence band is well approximated near $k=0$ by the diamondlike band structure^{38–40} (Fig. 5) and is described by the Luttinger Hamiltonian.^{41,42} When this Hamiltonian is combined with a spherical potential in the spherical band approximation, mixing between the bulk valence bands occurs.^{43,44} While this mixing is weak in bulk excitons,⁴³ it is significant in quantum dots.^{14,32,34–37} The main result is that parity and the total hole angular momentum, $F=L_h+J$, are the only good quantum numbers for the hole envelope function. L_h and J are not conserved. Quantum dot hole states have contributions from L_h and L_h+2 spherical harmonics, commonly referred to as ‘‘ S - D mixing,’’ as well as contributions from the heavy-hole, light-hole, and split-off valence subbands. The quantum dot hole states are labeled as $n_h L_F$, where L_F designates the combination of L and $L+2$ spherical harmonics, which have total angular momentum F . The electron envelope function, not affected by the valence-band complexities, is still labeled $n_e L_e$. In this notation the first excited pair state is labeled as $1S_{3/2}1S_e$ but contains the three hole components: ($F=3/2$, $J=3/2$, $L_h=0$), ($F=3/2$, $J=3/2$, $L_h=2$), and ($F=3/2$, $J=1/2$, $L_h=2$). A special notation is required for transitions involving the P -like hole states with $F=1/2$. These hole states are not affected by valence-band mixing and states arising from the light-hole subband ($1P_{1/2}^l$) must be distinguished from those from the split-off subband ($1P_{1/2}^{so}$).¹⁴

A rigorous treatment of the valence band is important not only for determination of pair state energies but also for selection rules. Quantum dot transition strengths are determined by the overlap between electron and hole envelope functions.¹ Due to the valence-band mixing, the simple selection rules of early theories, $\Delta n=0$ and $\Delta L=0$,¹ are no longer valid.³²

B. Calculations

We assign the features of Fig. 4 by calculating quantum dot transitions as a function of size using the effective mass theory of Ref. 14, which includes valence-band mixing and uses the Kane model^{40,45} to incorporate the nonparabolicity of the conduction band. While the hole calculations assume an infinite potential boundary condition, a finite barrier (V_e) is used for the much lighter electron to allow penetration into the surrounding matrix.⁴⁶

While our hole calculations strictly follow Ref. 14, a simplified boundary condition, better suited to our system, is used for the electron. Electron eigenvalues are evaluated by numerically solving the boundary condition⁴⁷

$$\left[1 + 2f + \frac{E_p}{3} \left(\frac{2}{E + E_g/2} + \frac{1}{E + E_g/2 + \Delta} \right) \right] \times \frac{\partial}{\partial r} \ln[j_l(k_s r)]|_{r=a} = \frac{\partial}{\partial r} \ln[K_l'(k_m r)]|_{r=a}, \quad (1)$$

which matches the semiconductor conduction band with the surrounding matrix. A simple free-electron form is assumed for the matrix, which in our samples is an organic solvent. Here a is the quantum dot radius, E_g is the semiconductor band gap, Δ is the spin-orbit coupling, $j_l(z)$ is the l th-order spherical Bessel function, and

$$K_l'(z) = (\pi/2z)^{1/2} K_{l+1/2}(z), \quad (2)$$

with $K_{l+1/2}(z)$ the modified Bessel function. The energy of the electron level (E) is measured from midgap. The wave vectors in the semiconductor (k_s) and matrix (k_m) are given by

$$k_s^2 = \frac{2m_0}{\hbar^2} [E - E_g/2] \left[1 + 2f + \frac{E_p}{3} \left(\frac{2}{E + E_g/2} + \frac{1}{E + E_g/2 + \Delta} \right) \right]^{-1}$$

and

$$k_m^2 = -\frac{2m_0}{\hbar^2} [E - V_e - E_g/2], \quad (3)$$

where m_0 is the free-electron mass. In these equations E_p and f are Kane model parameters which describe the conduction-band curvature. E_p (f) accounts for the influence of the valence band (higher bands) on the conduction band.⁴⁸ Since E_p and f are related to m_e , the effective mass of the electron at the bottom of the conduction band,⁴⁸ the electron levels are described by the parameters Δ , E_g , V_e , m_e , and E_p .

In any model the electron-hole Coulomb interaction is problematic because it cannot be addressed analytically. Within the strong confinement approximation the Coulomb term is typically included as a first-order energy correction. We correct pair states to first order by adjusting states that contain S_e (P_e) by $-1.8e^2/\epsilon a$ ($-1.7e^2/\epsilon a$), where ϵ is the semiconductor dielectric constant.² This approximation is used since a more rigorous approach is not necessary to assign the transitions. However, more detailed treatments by Koch and co-workers demonstrate that even in the strong confinement regime the Coulomb term can be important.^{37,49} In particular the electron-hole pair states are mixed by the Coulomb interaction. Since our assignments ignore this effect, the labels we use below are in reality only approximate. Consequences of the Coulomb mixing are discussed further below.

We use standard nonlinear least-squares methods³¹ to globally fit a subset of the experimental data. We use size estimates for our data and fit the $1S_{3/2}1S_e$, $2S_{3/2}1S_e$, and $1P_{3/2}1P_e$ transitions to features (a), (b), and (d) in Fig. 4. These transitions are chosen since they exhibit simple size-dependent behavior (no avoided crossings) and their assignment is relatively certain. Our fitting routine adjusts three

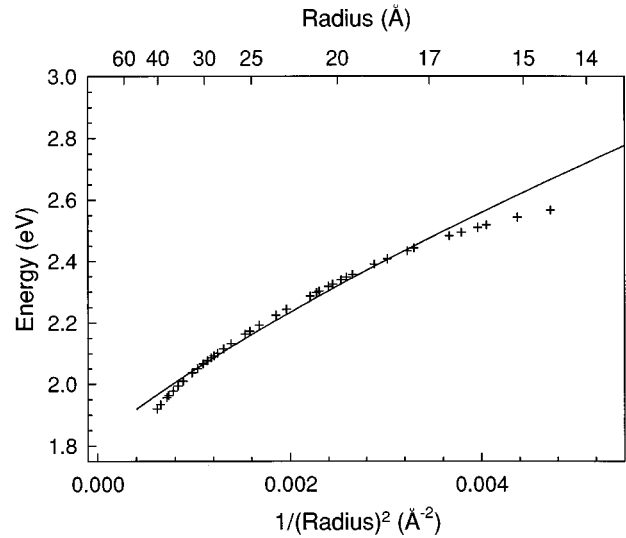


FIG. 6. Energy of the first excited state ($1S_{3/2}1S_e$) vs $1/\text{radius}^2$. The curve (solid line) obtained from theory is compared with PLE data (crosses).

parameters: the Luttinger band parameters γ_1 and γ_2 ,⁴² which describe the curvature of the three valence subbands, and the potential barrier for the electron, V_e . We use literature values for the parameters Δ , E_g , m_e , and E_p [$\Delta=0.42$ eV,⁵⁰ $E_g(10\text{ K})=1.839$ eV,⁵⁰ $m_e=0.11m_0$,¹⁴ $E_p=17.5$ eV (Ref. 14)]. Our best fit is obtained with $\gamma_1=2.04$ and $\gamma_2=0.58$, in close agreement with Ekimov *et al.*¹⁴ This corresponds to valence-band effective masses $m_{\text{hh}}=1.14$, $m_{\text{lh}}=0.31$, and $m_{\text{so}}=0.49$ for the heavy-hole, light-hole, and split-off subbands (Fig. 5). The ratio of light- to heavy-hole effective masses, β , is 0.28. The best fit also requires that $V_e=8.9$ eV. Although high, it is not surprising that this parameter is not physically meaningful. It depends strongly on the particular boundary condition assumed in Eq. (1). In addition it incorporates not only the finite barrier for the electron but all other deviations from the model. Therefore, while in theory this parameter describes the influence of the finite boundary condition on the electron, in practice V_e is used as a fitting parameter.

Figure 6 compares the calculated size dependence of the first excited state (solid line) with experimental data (crosses). The theoretical model reproduces the general trend of the experimental data, but not its curvature. Since the theory includes the nonparabolicity of the conduction band, the observed deviation implies that an additional “nonparabolicity” is present that is not accounted for by the theory. The most likely explanation for the deviation in small dots is the breakdown of the effective mass approximation. Another possibility is the simplistic choice for the quantum dot boundary condition, either infinite or square well. The data also diverge from theory at large sizes perhaps due to the increasing importance of the Coulomb interaction in the intermediate confinement regime. In any case, the discrepancy in the first transition is not large enough to keep us from our goal—assignment of the higher excited states.

The higher excited states are assigned by using the best fit parameters to calculate the energies of all allowed transitions ($n_h \leq 4$, $F_h \leq 5/2$) below feature (j) in Fig. 4, yielding ~ 60 transitions. The strength of each state is calculated and only

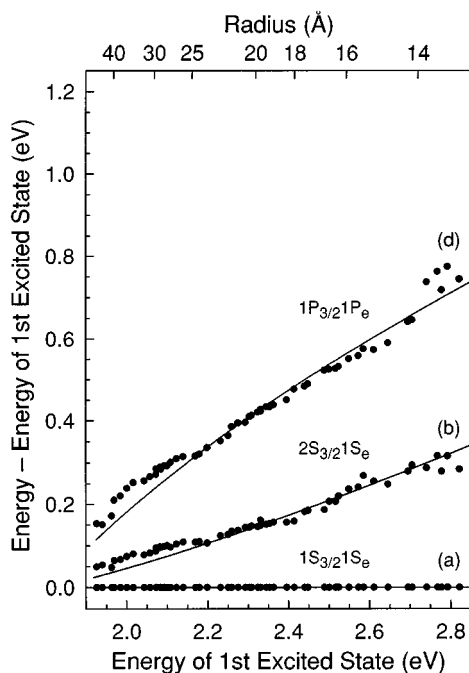


FIG. 7. Theoretically predicted pair states (solid lines) assigned to features (a), (b), and (d) in Fig. 4. The experimental data are shown for comparison (circles).

the strongest transitions are considered. Figures 7–10 show the best theoretical curves for features (a)–(j) from Fig. 4. Although the number of allowed states below feature (g) is fairly sparse and the assignments are relatively straightforward, the large density of allowed states prevents definitive assignment of features at higher energies.

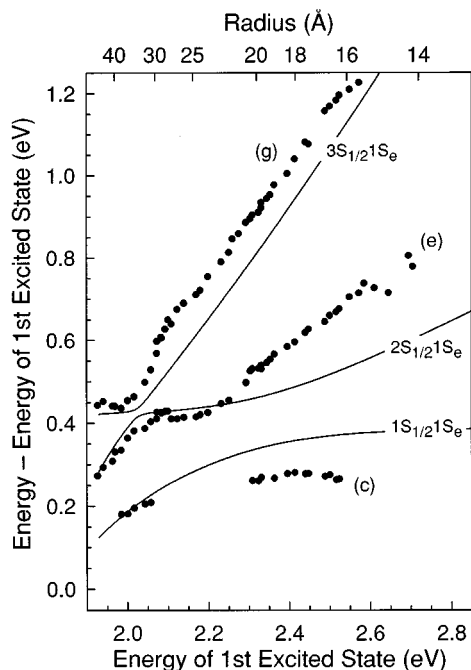


FIG. 8. Theoretically predicted pair states (solid lines) assigned to features (c), (e), and (g) in Fig. 4. The experimental data are shown for comparison (circles).

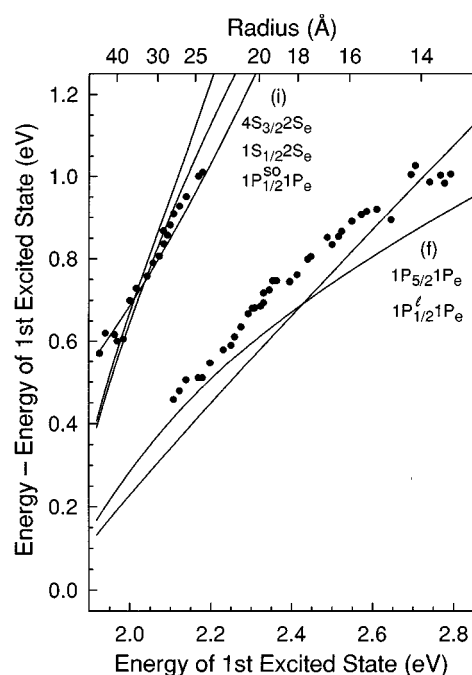


FIG. 9. Theoretically predicted pair states (solid lines), which are possible assignments for feature (f) and (i) in Fig. 4. The experimental data is shown for comparison (circles).

C. Assignments

Figure 7 compares features (a), (b), and (d) in Fig. 4 to the calculated $1S_{3/2}1S_e$, $2S_{3/2}1S_e$, and $1P_{3/2}1P_e$ transitions. The strong quantitative agreement between experiment and theory demonstrates the quality of the fitting procedure. These assignments are also consistent with intensity calculations, which indicate that $1S_{3/2}1S_e$ and $1P_{3/2}1P_e$ should be two of the strongest transitions, as observed. $2S_{3/2}1S_e$ should be weaker but clearly resolved due to its spectral isolation. These properties are demonstrated in Fig. 3 where features (a) ($1S_{3/2}1S_e$) and (d) ($1P_{3/2}1P_e$) dominate the spectrum while the weaker feature (b) ($2S_{3/2}1S_e$) is observed between them.

Figure 8 assigns features (c), (e), and (g) to $1S_{1/2}1S_e$, $2S_{1/2}1S_e$, and $3S_{1/2}1S_e$, respectively. An avoided crossing between the $2S_{1/2}1S_e$ and $3S_{1/2}1S_e$ states, which was initially reported in our preliminary results,¹⁶ is now unambiguously observed at ~ 2.0 eV. In addition we now observe a repulsion between the $1S_{1/2}1S_e$ and $2S_{1/2}1S_e$ states above 2.2 eV. Both avoided crossings are predicted by theory and their presence in the data is strong support for our assignments. However, Fig. 8 demonstrates that theory underestimates the repulsion in both avoided crossing regions, causing theoretical deviations in the predictions of the $1S_{1/2}1S_e$ and $2S_{1/2}1S_e$ states. The Coulomb mixing of the pair states, ignored by the model, couples the $n_h S_{1/2}1S_e$ transitions such that these states “push off” each other more strongly. The Coulomb term also causes $1S_{1/2}1S_e$ and $2S_{1/2}1S_e$ to avoid one another through their individual repulsion from the strongly allowed $1P_{3/2}1P_e$ [feature (d)], which lies between them. Because of these deviations from theory feature (d) was incorrectly assigned to $1S_{1/2}1S_e$ in our Letter.¹⁶ The more complete data set now suggests that it is more reason-

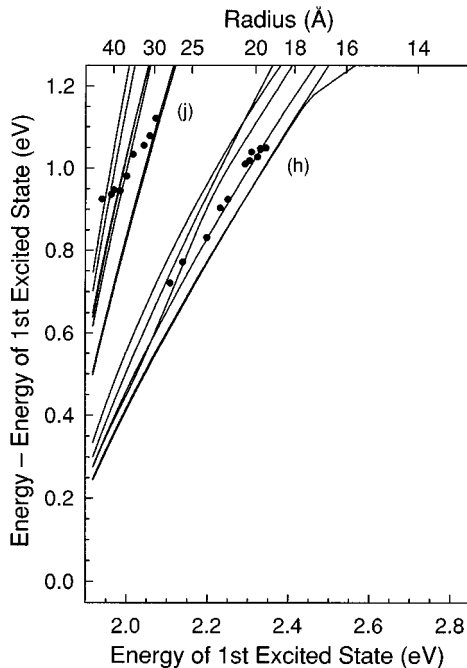


FIG. 10. Theoretically predicted pair states (solid lines), which are possible assignments for feature (h) ($1S_{1/2}1D_e$, $2S_{3/2}2S_e$, $1S_{3/2}2S_e$, $2S_{3/2}1D_e$, $1D_{5/2}1D_e$, and $4P_{3/2}1P_e$) and (j) ($2P_{1/2}^12P_e$, $3S_{3/2}3S_e$, $2P_{3/2}2P_e$, $4P_{3/2}2P_e$, $2P_{5/2}2P_e$, $4P_{5/2}2P_e$, and $3S_{3/2}2D_e$) in Fig. 4. The experimental data are shown for comparison (circles).

able to assign feature (c), not observed in the TDA data,¹⁶ to $1S_{1/2}1S_e$. Feature (d) is now assigned to the $1P_{3/2}1P_e$ state, as discussed above.

The behavior of the $n_h S_{1/2}1S_e$ transitions demonstrates the importance of valence-band structure in CdSe quantum dots since the avoided crossings are intimately related to the valence-band mixing. Like the $S_{3/2}$ hole state, $S_{1/2}$ is a mixture of $L_h=0$ and $L_h=2$ components due to S - D mixing. However, in $S_{1/2}$ the S and D components arise from different valence subbands. The D component comes from the $J=3/2$ band and the S component, which carries the oscillator strength, comes from the split-off $J=1/2$ band (Fig. 5). In the absence of valence-band mixing, the first S -type hole envelope function from the split-off band would cause a $1S_h1S_e$ -like pair state to appear 0.42 eV [the spin-orbit coupling in CdSe (Ref. 50)] above the first excited state. In Fig. 4 this transition would appear as a nearly horizontal line at 0.42 eV. States containing D -type hole envelope functions from the $J=3/2$ bands, which carry no oscillator strength, would cross this “spin-orbit line.” Once valence-band mixing is considered, the intersection of these S and D states is forbidden and avoided crossings result. Below 2.0 eV in Fig. 8 the $3S_{1/2}1S_e$ transition is mostly a $1S_h1S_e$ -like pair state from the split-off band ($J=1/2$) and the $2S_{1/2}1S_e$ and $3S_{1/2}1S_e$ states are mostly D -like hole states that try to cross the spin-orbit line.

The valence-band mixing also implies that the hole character of the $n_h S_{1/2}1S_e$ states changes after an avoided crossing. When the theoretical model outlined above is used to calculate quantum dot eigenfunctions,¹⁴ we find that the $2S_{1/2}$ hole state is 70% D -like for 60-Å-radius dots. After the

avoided crossing with $3S_{1/2}$ the hole component becomes 97% S -like for 25-Å-radius dots. The S character of $2S_{1/2}$ then falls again to 67% at 10-Å radius due to the interaction with the D -like $1S_{1/2}$. Such changes are important because they influence the strength of the observed transitions. In large dots $1S_{1/2}$ is mostly D -like (>80%). The $1S_{1/2}1S_e$ transition is then weakly observed due to the poor overlap of $1S_{1/2}$ with $1S_e$. However, as mixing with $2S_{1/2}$ increases, $1S_{1/2}$ becomes more S -like with decreasing dot size. This explains why experimentally $1S_{1/2}1S_e$ [feature (c)] increases in intensity with decreasing size. Although appearing as a subtle shoulder on $1P_{3/2}1P_e$ in the largest sizes, it is clearly resolved in the ~18-Å radius sample shown in Fig. 3. With decreasing size $1S_{1/2}1S_e$ gains strength, eventually merging with the stronger $2S_{3/2}1S_e$ transition (Fig. 4).

The agreement between theory and data in Figs. 6–8 allows us to be confident in the assignment of the features discussed above ($1S_{3/2}1S_e$, $2S_{3/2}1S_e$, $1P_{3/2}1P_e$, $1S_{1/2}1S_e$, $2S_{1/2}1S_e$, and $3S_{1/2}1S_e$). The increasing density of allowed states at high confinement energy makes the remaining assignments more difficult. Figures 9 and 10 present possibilities for features (f), (h), (i), and (j) in Fig. 4. We assign (f) to $1P_{1/2}^11P_e$ and/or $1P_{5/2}1P_e$ (Fig. 9). These transitions best reproduce the behavior of (f), which begins near the avoided crossing of $2S_{1/2}1S_e$ and $3S_{1/2}1S_e$. Figure 9 also shows the best assignments for feature (i): $1P_{1/2}^{s0}1P_e$, $4S_{3/2}2S_e$, and/or $1S_{1/2}2S_e$. $1P_{1/2}^{s0}1P_e$ shows the best agreement with the data, but all three transitions are expected to be strongly allowed. Figure 10 presents possible assignments for feature (h) ($1S_{1/2}1D_e$, $2S_{3/2}2S_e$, $1S_{3/2}2S_e$, $2S_{3/2}1D_e$, $1D_{5/2}1D_e$, and $4P_{3/2}1P_e$) and for feature (j) ($2P_{1/2}^12P_e$, $3S_{3/2}3S_e$, $2P_{3/2}2P_e$, $4P_{3/2}2P_e$, $2P_{5/2}2P_e$, $4P_{5/2}2P_e$, and $3S_{3/2}2D_e$). To assign features (h) or (j) to one of these states is impossible and potentially misleading since the eigenstates yielding (h) and (j) are likely to be mixtures of these states.

D. Additional complications

Each theoretical pair state shown in Figs. 6–10 is a single, but highly degenerate, state. In reality additional terms in the Hamiltonian, which for simplicity have been neglected in the above model, partially lift the degeneracies. For example, while the model assumes that the dots are spherically shaped crystallites with cubic (zinc-blende) lattice symmetry, structural studies show that the dots are slightly prolate (aspect ratio 1.0–1.3) with a hexagonal (wurtzite) crystal lattice.¹⁵ These physical attributes^{51,52} along with the Coulomb term^{37,49} and the exchange interaction between the electron and hole^{53–56} lead to exciton fine structure. However, the above model remains valid since these effects are sufficiently small to be treated as perturbations.⁵⁶ Therefore, although the fine structure implies that each transition shown in Figs. 7–10 is actually a multiplet of sublevels, such splittings are generally not observed, probably due to variations in sublevel spacings caused by size, shape, and structural inhomogeneities along with broad sublevel linewidths. In fact these effects have been commonly ignored since they are not necessary to explain most results.

However, for our present data, the exciton fine structure may be important for two reasons. First, as discussed in our companion paper,²⁹ the fine structure is consistent with the band-edge structure observed in our PLE and TDA results.

Second, the splittings may be responsible for some portion of the observed transition linewidths. The observation that linewidths increase with increasing energy, commonly explained by lifetime broadening, may result from the fact that higher transitions have higher angular momentum and may exhibit broader widths due to the increased complexity of their multiplets. In this case states with low angular momentum would be more likely to be resolved. For example, of the two possible assignments shown in Fig. 9 for feature (f), $1P'_{1/2}1P_e$ is 12-fold degenerate before consideration of multiplet splittings while $1P_{5/2}1P_e$ is initially 36-fold degenerate. (For comparison the dominant $n_hS_{1/2}1S_e$ and $n_hS_{3/2}1S_e$ transitions are initially fourfold and eightfold degenerate, respectively.) If both transitions have similar oscillator strength and if their multiplet width is proportional to their initial degeneracy, $1P'_{1/2}1P_e$ would ride above a much broader and unresolved $1P_{5/2}1P_e$. $1P'_{1/2}1P_e$ would then be responsible for feature (f). This description, in which high angular momentum transitions are concealed by overlapping low angular momentum states, is also consistent with our fits (Fig. 3), which require an effective continuum (cubic background) to represent underlying transitions that are not resolved.

V. CONCLUSION

In this paper we address one of the original and basic questions about quantum dots—how their electronic spectra

evolve with size in the strong confinement regime. We present the size dependence of ten absorption features observed in CdSe quantum dots ranging from ~ 12 to ~ 53 Å in radius. By comparing the experimental results with effective mass calculations, we find sufficient agreement between theory and experiment to confidently assign six transitions and present possible assignments for the remaining four. Avoided crossings in the $n_hS_{1/2}1S_e$ transitions, predicted by theory, are clearly present in our data and demonstrate the importance of valence-band structure in the description of the quantum dot pair states. Quantitative differences between experiment and theory suggest that the model would be further improved by a more rigorous treatment of the Coulomb interaction.

ACKNOWLEDGMENTS

We thank Al. L. Efros for extremely helpful comments and discussions. We also wish to thank A. Sacra for help with the analysis and C. B. Murray and M. Nirmal for assistance in sample preparation. D.J.N. benefited from support from NSF and Arthur D. Little. M.G.B. thanks the Lucille and David Packard Foundation and the Alfred P. Sloan Foundation for support. This work was funded in part by the NSF-MRSEC program (DMR-94-00334) and by NSF (DMR-91-57491 and ECS-91-18907). We also thank the MIT Harrison Spectroscopy Laboratory (NSF-CHE-93-04251) for use of its facilities.

*Present address: University of California, San Diego, 9500 Gilman Drive, La Jolla, CA 92093-0340.

¹Al. L. Efros and A. L. Efros, *Fiz. Tekh. Poluprovodn.* **16**, 1209 (1982) [*Sov. Phys. Semicond.* **16**, 772 (1982)].

²L. E. Brus, *J. Chem. Phys.* **80**, 4403 (1984).

³A. I. Ekimov, Al. L. Efros and A. A. Onushchenko, *Solid State Commun.* **56**, 921 (1985).

⁴A. I. Ekimov and A. A. Onushchenko, *Pis'ma Zh. Eksp. Teor. Fiz.* **40**, 337 (1984) [*JETP Lett.* **40**, 1136 (1984)].

⁵R. Rossetti, R. Hull, J. M. Gibson, and L. E. Brus, *J. Chem. Phys.* **82**, 552 (1985).

⁶A. I. Ekimov, A. A. Onushchenko, and Al. L. Efros, *Pis'ma Zh. Eksp. Teor. Fiz.* **43**, 292 (1986) [*JETP Lett.* **43**, 376 (1986)].

⁷N. Chestnoy, R. Hull, and L. E. Brus, *J. Chem. Phys.* **85**, 2237 (1986).

⁸A. P. Alivisatos, A. L. Harris, N. J. Levinos, M. L. Steigerwald, and L. E. Brus, *J. Chem. Phys.* **89**, 4001 (1988).

⁹A. I. Ekimov, Al. L. Efros, M. G. Ivanov, A. A. Onushchenko, and S. K. Shumilov, *Solid State Commun.* **69**, 565 (1989).

¹⁰Y. Wang and N. Herron, *Phys. Rev. B* **42**, 7253 (1990).

¹¹M. G. Bawendi, W. L. Wilson, L. Rothberg, P. J. Carroll, T. M. Jedju, M. L. Steigerwald, and L. E. Brus, *Phys. Rev. Lett.* **65**, 1623 (1990).

¹²N. Peyghambarian, B. Fluegel, D. Hulin, A. Migus, M. Joffre, A. Antonetti, S. W. Koch, and M. Lindberg, *IEEE J. Quantum Electron.* **25**, 2516 (1989).

¹³V. Esch, B. Fluegel, G. Khitrova, H. M. Gibbs, X. Jiajin, K. Kang, S. W. Koch, L. C. Liu, S. H. Risbud, and N. Peyghambarian, *Phys. Rev. B* **42**, 7450 (1990).

¹⁴A. I. Ekimov, F. Hache, M. C. Schanne-Klein, D. Ricard, C. Flytzanis, I. A. Kudryavtsev, T. V. Yazeva, A. V. Rodina, and

Al. L. Efros, *J. Opt. Soc. Am. B* **10**, 100 (1993).

¹⁵C. B. Murray, D. J. Norris, and M. G. Bawendi, *J. Am. Chem. Soc.* **115**, 8706 (1993).

¹⁶D. J. Norris, A. Sacra, C. B. Murray, and M. G. Bawendi, *Phys. Rev. Lett.* **72**, 2612 (1994).

¹⁷D. J. Norris, M. Nirmal, C. B. Murray, A. Sacra, and M. G. Bawendi, *Z. Phys. D* **26**, 355 (1993).

¹⁸M. Nirmal, C. B. Murray, and M. G. Bawendi, *Phys. Rev. B* **50**, 2293 (1994).

¹⁹W. Hoheisel, V. L. Colvin, C. S. Johnson, and A. P. Alivisatos, *J. Chem. Phys.* **101**, 8455 (1994).

²⁰C. R. M. de Oliveira, A. M. de Paula, F. O. Plentz Filho, J. A. Medeiros Neto, L. C. Barbosa, O. L. Alves, E. A. Menezes, J. M. M. Rios, H. L. Fragnito, C. H. Brito Cruz, and C. L. Cesar, *Appl. Phys. Lett.* **66**, 439 (1995).

²¹P. A. M. Rodrigues, G. Tamulaitis, P. Y. Yu, and S. H. Risbud, *Solid State Commun.* **94**, 583 (1995).

²²D. J. Norris and M. G. Bawendi, *J. Chem. Phys.* **103**, 5260 (1995).

²³M. Chamorro, C. Gourdon, P. Lavallard, and A. I. Ekimov, *Jpn. J. Appl. Phys. Suppl.* **34-1**, 12 (1995).

²⁴The bulk exciton Bohr radius in CdSe is 56 Å.

²⁵L. R. Becerra, C. B. Murray, R. G. Griffin, and M. G. Bawendi, *J. Chem. Phys.* **100**, 3297 (1994).

²⁶J. E. Bowen Katari, V. L. Colvin, and A. P. Alivisatos, *J. Phys. Chem.* **98**, 4109 (1994).

²⁷Sizes reported are estimated from extensive size-dependent transmission electron microscopy (TEM) and small-angle x-ray measurements and are based on the energy of the first absorption peak.

²⁸C. B. Murray, Ph.D. thesis, Massachusetts Institute of Technology, 1995.

- ²⁹D. J. Norris, Al. L. Efros, M. Rosen, and M. G. Bawendi, following paper, *Phys. Rev. B* **53**, 16 347 (1996).
- ³⁰D. J. Norris, Ph.D. thesis, Massachusetts Institute of Technology, 1995.
- ³¹W. H. Press, B. P. Flannery, S. A. Teukolsky, and W. T. Vetterling, *Numerical Recipes in C* (Cambridge University Press, Cambridge, 1988), Chap. 14.
- ³²J. B. Xia, *Phys. Rev. B* **40**, 8500 (1989).
- ³³C. Kittel, *Quantum Theory of Solids* (Wiley, New York, 1987), Chap. 14.
- ³⁴G. B. Grigoryan, E. M. Kazaryan, Al. L. Efros, and T. V. Yazeva, *Fiz. Tverd. Tela* **32**, 1772 (1990) [*Sov. Phys. Solid State* **32**, 1031 (1990)].
- ³⁵K. J. Vahala and P. C. Sercel, *Phys. Rev. Lett.* **65**, 239 (1990).
- ³⁶P. C. Sercel and K. J. Vahala, *Phys. Rev. B* **42**, 3690 (1990).
- ³⁷S. W. Koch, Y. Z. Hu, B. Fluegel, and N. Peyghambarian, *J. Cryst. Growth* **117**, 592 (1992).
- ³⁸R. H. Parmenter, *Phys. Rev.* **100**, 573 (1955).
- ³⁹G. Dresselhaus, *Phys. Rev.* **100**, 580 (1955).
- ⁴⁰E. O. Kane, *J. Phys. Chem. Solids* **1**, 249 (1957).
- ⁴¹J. M. Luttinger and W. Kohn, *Phys. Rev.* **97**, 869 (1955).
- ⁴²J. M. Luttinger, *Phys. Rev.* **102**, 1030 (1956).
- ⁴³A. Baldereschi and N. O. Lipari, *Phys. Rev. B* **8**, 2697 (1973).
- ⁴⁴In the spherical band approximation, outlined in Ref. 43 for the charged impurity problem, only terms of spherical symmetry in the Luttinger Hamiltonian are considered in first order. Cubic “warping” terms are neglected but may be added as a small perturbation.
- ⁴⁵C. R. Pidgeon and R. N. Brown, *Phys. Rev.* **146**, 575 (1966).
- ⁴⁶D. B. Tran Thoai, Y. Z. Hu, and S. W. Koch, *Phys. Rev. B* **42**, 11 261 (1990).
- ⁴⁷Al. L. Efros (private communication).
- ⁴⁸R. L. Aggarwal, in *Semiconductors and Semimetals*, edited by R. K. Willardson and A. C. Beer (Academic, New York, 1972), Vol. 9, p. 151.
- ⁴⁹Y. Z. Hu, M. Lindberg, and S. W. Koch, *Phys. Rev. B* **42**, 1713 (1990).
- ⁵⁰*Semiconductors. Physics of II-VI and I-VII Compounds, Semimagnetic Semiconductors*, edited by K. H. Hellwege, Landolt-Börnstein, New Series, Group III, Vol. 17, Pt. b (Springer-Verlag, Berlin, 1982).
- ⁵¹Al. L. Efros, *Phys. Rev. B* **46**, 7448 (1992).
- ⁵²Al. L. Efros and A. V. Rodina, *Phys. Rev. B* **47**, 10 005 (1993).
- ⁵³S. Nomura, Y. Segawa, and T. Kobayashi, *Phys. Rev. B* **49**, 13 571 (1994).
- ⁵⁴T. Takagahara, *Phys. Rev. B* **47**, 4569 (1993).
- ⁵⁵P. D. J. Calcott, K. J. Nash, L. T. Canham, M. J. Kane, and D. Brumhead, *J. Lumin.* **57**, 257 (1993).
- ⁵⁶M. Nirmal, D. J. Norris, M. Kuno, M. G. Bawendi, Al. L. Efros, and M. Rosen, *Phys. Rev. Lett.* **75**, 3728 (1995).